# Combustion synthesized Fe doped CeO2 powder-characterization, optical absorption and EPR spectroscopy

*by* Ahmad Saiful Haqqi

J Mater Sci: Mater Electron
DOI 10.1007/s10854-016-4323-x

# Combustion synthesized Fe doped $CeO_2$ powder-characterization, optical absorption and EPR spectroscopy

Vijay Singh[1] · G. Sivaramaiah[2] · J. L. Rao[3] · N. Singh[1] · Anoop K. Srivastava[4] · Pramod K. Singh[5] · S. U. Pawar[6] · H. Gao[1] · P. Mardina[1]

Received: 9 November 2015 / Accepted: 11 January 2016


**Abstract** Fe doped $CeO_2$ powder was prepared using solution combustion method. Powder X-ray diffraction and scanning electron microscopy methods are used to characterize the combustion derived powder. The optical absorption spectrum exhibits three bands due to $Fe^{3+}$ and $Fe^{2+}$ ions. Electron paramagnetic resonance (EPR) spectrum of this sample exhibits number of resonance signals due to $Fe^{3+}$ ions. The number of spins (N) participating in resonance and its paramagnetic susceptibility ($\chi$) has been evaluated. From EPR and optical studies it is observed that iron ions are present in trivalent state.

## 1 Introduction

Among the various rare-earth based oxide materials $CeO_2$ is the most promising rare earth oxide which has been the popular subject of research. Since $CeO_2$ endows with some exceptional features such as a thinner interfacial layer, higher capacitance value, high dielectric constant, high effective electric field across the tunnelling oxide and lower leakage current, therefore it is being used extensively in semiconductor fabrication over the past few years [1–5]. $CeO_2$ based rare earth oxide ceramics have wide range of applications in the field of laser glass, integral optical instruments, fluorescent lamps and so on [2–8]. $CeO_2$ has been studied under the photonic band gap materials and has become a popular subject of interests in the research area.

There are several researches being carried out based on the preparations and properties of heterogeneous photo catalyst $CeO_2$ coupled with other materials throughout last decade [8–10]. $CeO_2$ has been proved as an excellent photo catalyst in the modern catalytic industry because of its high photocatalytic activity, low cost and environment friendly behaviour [11–13]. As compared to all other stabilized zirconia system, $CeO_2$ stabilized zirconia is considered to have an excellent thermal stability and high toughness. Ceria derived oxides, especially Zr doped cerium oxides have drawn the significant attention of researchers and intensive studies reported on them for past several years [14–16]. An intensive study of electrical conductivity and defect structure of $CeO_2$–$ZrO_2$ mixed oxide has been done by Lee et al. [17]. Wang et al. [18] have reported the preparation of inverse opal cerium dioxide for optical properties research. Luisetto et al. [19] have investigated the catalytic performances of Ni/$CeO_2$–$Al_2O_3$ catalysts for the dry reforming of methane. Due to some peculiar redox properties and variable valence states (4+ and 3+), ceria and ceria derived oxides play an important role as a heterogeneous catalyst in the field of industrial applications such as water gas shift reactions, solid oxide fuel cells anodes, automotive three way exhaust, etc. [20–23].

It was found that photocatalytic properties of $CeO_2$ nanomaterials can be improved further by doping with

✉ Vijay Singh
vijayjiin2006@yahoo.com

1 Department of Chemical Engineering, Konkuk University, Seoul 143-701, Korea
2 Department of Physics, Government College for Men (A), Kadapa 516 004, India
3 Department of Physics, Sri Venkateswara University, Tirupati 517 502, India
4 Division of Electronics Engineering, Chonbuk National University, Jeonju, Jeonbuk 561-756, Korea
5 Materials Research Laboratory, Sharda University, Greater Noida 201310, India
6 Department of Physics, Shri Shivaji Mahavidyalaya, Barshi, Solapur 413411, India

Published online: 19 January 2016

transition metal (Fe), which enhances the oxygen storage capacity of ceria lattice [24]. Fe doped $CeO_2$ nano particles have emerged as efficient photocatalysts in the visible region for dye waste water treatment and for pigmented ultraviolet filter applications [25]. Tiebao et al. [26] have investigated the fabrication of nano $CeO_2$ and application of nano $CeO_2$ in Fe matrix composites. Influence of $Fe^{3+}$ doping on optical properties of $CeO_2$ nanopowders, has been discussed by Radović et al. [27]. Wang et al. [28] have reported the enhanced photocatalytic performance of ordered mesoporous Fe doped $CeO_2$ catalysts for the reduction of $CO_2$ with $H_2O$ under simulated solar irradiation. From the above several reports, it appears that cerium oxides have different potential applications and been used as catalysts, phosphors, polishing materials, fuel cells, gas sensors and so on in various technological fields. It is well known that, among the different valence states of Fe, the trivalent state is the most stable one. $Fe^{3+}$ ions have significant use as active media in solid state optical materials/display/lasers devices etc. These ions interact well with the host lattice and therefore are widely investigated for numerous optical spectroscopic properties. Furthermore, $Fe^{3+}$ ion is interesting because of its extreme sensitivity towards optical and electron paramagnetic resonance (EPR) properties and their dependency on the nature of the host matrix. Although there are plenty of literature reports available on the doped and un-doped $CeO_2$, there are only some reports on Fe doped $CeO_2$ materials.

Further, $CeO_2$ is being used in phosphor systems to improve the luminescence properties of material by either mixing or coating. However, $CeO_2$ as a host for the Fe ions doping has not been often reported. In view of this, in this work, we have selected $CeO_2$ as a host material for the transition metal ions. The addition of transition metal ions to the inorganic oxide material changes them to exhibit the structural, chemical, and physical behavior. Among the transition metal oxides, iron is of much interest in the contemporary and emerging technology, wherein it finds applications in the fields like microelectronics, solid state ionics etc. It is noticed that electron paramagnetic resonance (EPR) is used as a tool for the characterization of rare earth and transition metal ions in optical and laser crystals, because of their relevance in optoelectronic devices. EPR spectra of $Fe^{3+}$ ions in various glasses have been extensively recorded and studied [29, 30]. Accordingly, $Fe^{3+}$ is a very useful probe to obtain the information about local environment in the host lattice [31–33]. To the best of our knowledge, no details regarding the optical properties of Fe doped $CeO_2$ have been reported in the literature. It is widely accepted that the EPR is an amenable method for elucidating the ground state properties of transition metal ions. In this context, we have studied the Fe doped $CeO_2$ using optical and EPR spectroscopic techniques. It will be interesting to understand the site symmetry of Fe when incorporated into $CeO_2$ matrix.

The Fe doped $CeO_2$ sample was prepared by combustion route. The advantages of this synthesis method are possibility to prepare good homogeneity through mixing at the molecular level, safe, easy and no requirement of any special arrangements for preparation. In the present work a detailed investigation on cerium oxide doped with iron has been undertaken using spectroscopic methods such as X-ray diffraction (XRD), scanning electron microscopy (SEM), electron paramagnetic resonance (EPR), optical absorption and the results obtained from these studies are discussed.

## 2 Experimental details

### 2.1 Synthesis

We prepared sample of Fe doped $CeO_2$ utilizing the combustion process. In a typical synthesis, 4 g of $Ce(NO_3)_3{\cdot}6H_2O$, 0.0744 g of $Fe(NO_3)_3{\cdot}9H_2O$ and 1.4 g of urea ($NH_2CONH_2$) was dissolved in a minimum quantity of deionized water in a China dish with 300 ml capacity to obtain a homogeneous solution. The solution was then transferred into a furnace preheated to 550 °C. The water quickly evaporated and the mixture formed foam, within which a vigorous reaction between the nitrates and urea soon initiated and ended. The entire combustion process was completed in about 3–5 min. The resultant fluffy masses were crushed into a fine powder. Then the powder was transferred to a 50 ml alumina crucible to be heat-treated at 1000 °C for 2 h in air to remove by-products and reduce internal strains before it was used for further characterization.

### 2.2 Characterization

Powder XRD pattern was recorded in the 2θ range from 10° to 80° on a Philips X'Pert X-ray diffractometer with graphite monochromatized $CuK_\alpha$ radiation and nickel filter at a scanning step of 0.03°. The morphology of the prepared sample was investigated using SEM on Hitachi S-3200N instrument. The UV–Vis absorption spectrum of sample was measured in diffuse reflectance mode using a Cary 6000i UV–Vis–NIR spectrophotometer equipped with an integrating sphere. A powdered sample of 100 mg was taken in a quartz tube for the EPR measurements. The EPR spectra of sample were recorded on a JEOL FE1X EPR Spectrometer, operating in the X-band frequencies, with a field modulation of 100 kHz.

## 3 Results and discussion

### 3.1 X-ray diffraction analysis

XRD measurements were carried out for analyzing crystal structure and its phase. The XRD pattern of combustion derived Fe doped $CeO_2$ powder has been measured and is shown in Fig. 1. These results show the sample to exhibit face-centered cubic fluorite crystal structure belonging to space group *Fm3m* (No. 225). The fluorite structure with the crystalline planes of (111), (200), (220), (311), (222), (400), (331) and (420) are matched with that of pure $CeO_2$ (JCPDS, File No. 34-0394). Figure 1 shows that doping with $Fe^{3+}$ ions has no effect on shapes and position of diffraction peaks. Moreover, there is no additional signature in XRD pattern of Fe doped $CeO_2$ powders which imply that the dopant was incorporated into the $CeO_2$ structure, which indicates the formation of single phased $CeO_2$. This XRD analysis indicated that the dopant do not participate in overall crystal formation except replacing of Ce/sitting between few atoms. The average crystallite size of the Fe doped $CeO_2$ sample was estimated by using Scherrer's method, $d = k\lambda/\beta \cos\theta$, where k is a constant which is equal to 0.89, $\beta$ is the full width at half maxima in radians, $\lambda$ is the wavelength of X-ray and $\theta$ is the Bragg's angle. The average crystallite size was found to be 48 nm.

### 3.2 Morphological analysis

SEM study was carried out to investigate the morphology of the synthesized powder. Figure 2 displays higher magnification SEM image of the Fe doped $CeO_2$ powder. SEM studies showed that, there is a cluster of large number of sphere like balls. There is no uniformity in distribution of particle; as almost all the smaller particles in a cluster look alike. The non-uniform behavior of the particles can be attributed to the non-uniform distribution of temperature and mass flow in the combustion flame.

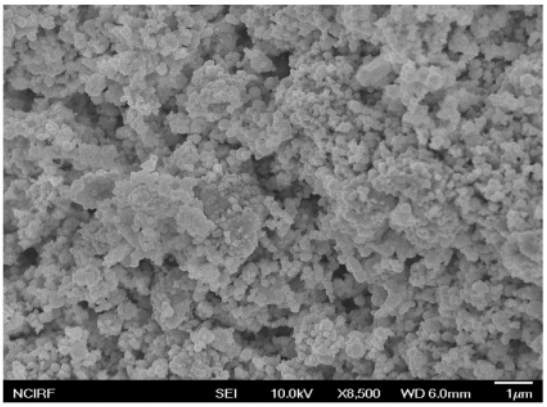


**Fig. 2** SEM micrograph of $CeO_2$:$Fe^{3+}$

### 3.3 Absorption analysis

The absorption spectrum of Fe doped $CeO_2$ sample is shown in Fig. 3. From the figure it is evident that two broad bands have been observed at around 535 nm (18,692 $cm^{-1}$) and 906 nm (11,037 $cm^{-1}$). The band at around 535 nm (18,692 $cm^{-1}$) has been attributed to $Fe^{3+}$ ions in octahedral symmetry and assigned to the transition $^6A_{1g}(S) \rightarrow {}^4T_{2g}(G)$ [32]. The weak band at around 671 nm (14,903 $cm^{-1}$) has been attributed to $Fe^{3+}$ ions in octahedral symmetry and assigned to the transition $^6A_{1g}(S) \rightarrow {}^4T_{1g}(G)$. The band at around 906 nm (11,037 $cm^{-1}$) has been attributed to $Fe^{2+}$ ions and assigned to the transition $^5E(D) \rightarrow {}^5T_2(D)$ in tetrahedral symmetry [33]. For $Fe^{3+}$ ions, spin-forbidden transitions are allowed. Therefore the intensity of the bands should be low. In the present case, two or more bands due to $Fe^{3+}$ ions were merged into one band and resulted a broad band at around 535 nm (18,692 $cm^{-1}$). For $Fe^{2+}$ ions, spin-allowed transitions are possible. Therefore a broad band is resulted at around 906 nm (11,037 $cm^{-1}$). For iron 2+, 3+, 4+ even higher oxidation

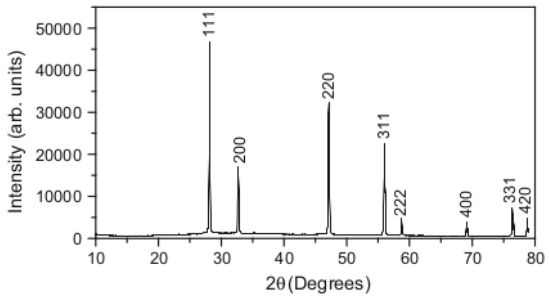


**Fig. 1** Powder XRD pattern of $CeO_2$:$Fe^{3+}$

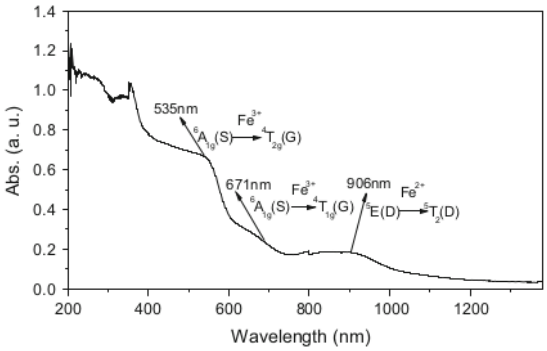


**Fig. 3** Absorption spectrum of $CeO_2$:$Fe^{3+}$

states are found to occur. Among these 3+ oxidation state is more stable for iron. But $Fe^{2+}$ and $Fe^{3+}$ are optically active in this sample. During sample preparation, some of the $Fe^{3+}$ ions are converted into $Fe^{2+}$ ions. In general, experimental data cannot be interpreted correctly in terms of 3+ oxidation state alone, but have to be analysed in view of the coexistence of Fe ions of different vacancies. In the next section, $Fe^{2+}$ ions were not observed in EPR studies. Mehdikhani and Borhani [34] studied optical spectroscopy of sodium silicate glasses prepared with nano and micro sized iron oxide particles. They observed three bands at around 380, 420, 435 nm due to $Fe^{3+}$ ions. They also observed a broad band at around 1050 nm due to $Fe^{2+}$ ions. Klement et al. [35] studied spectroscopic analysis of iron doped glasses. They observed two bands at around 5000 and 10,000 $cm^{-1}$. These bands were due to $Fe^{2+}$ ions and assigned to the transitions $^5T_2(D) \rightarrow {}^5E(D)$ and $^5E(D) \rightarrow {}^5T_2(D)$ in octahedral and tetrahedral symmetries, respectively. In view of the above information the band at around 906 nm is most likely due to $Fe^{2+}$ ions. Singh et al. [36] studied optical absorption studies of $Fe_2O_3$ and $CeO_2$ doped glasses. They observed two week bands at around 408 and 424 nm due to $Fe^{3+}$ ions in octahedral symmetry. They also observed two bands at around 411 and 431 nm due to excitons for $CeO_2$ doped glasses. The bands located between 200 and 350 nm are the host absorption bands due to charge transfer (CT) from $O^{2-}$ to $Ce^{4+}$, because of the energy gap between O(2*p*) band and Ce(4*f*) is in the range of 6–8 eV [37, 38].

### 3.4 EPR studies

EPR spectrum of un-doped does not show any absorption signals. This indicates that the starting materials do not contain any paramagnetic impurities and defects. When Fe is added to the $CeO_2$ as dopant, then this exhibits resonance signals due to $Fe^{3+}$ ions. Figure 4a shows EPR spectrum of $CeO_2$:$Fe^{3+}$ at RT. This spectrum exhibits the effective g values at g = 7.77, 4.05, 2.07 and 1.93. Figure 4b shows the EPR spectrum of $CeO_2$:$Fe^{3+}$ at 110 K. This spectrum gives the effective g values at g = 24.92, 7.79, 4.17, 2.71, 2.21 and 2.01. These large g values are present when certain symmetry elements are present. The large g values are usually expressed by spin-Hamiltonian of the form [39]

$$H_s = g\beta HS + D\left[S_z^2 - (1/3)\,S(S+1)\right] + E\left(S_x^2 - S_y^2\right) \quad (1)$$

where the terms involving D and E are the axial and orthorhombic crystal-field components respectively, S is the spin operator and g is the spectroscopic splitting factor. Free $Fe^{3+}$ ions belong to the $d^5$ configuration with $^6S_{5/2}$ as the ground state, without any spin–orbit interaction. The g value of free $Fe^{3+}$ ions is expected to lie very close to the free-electron value of 2.0023. The experimental g values of

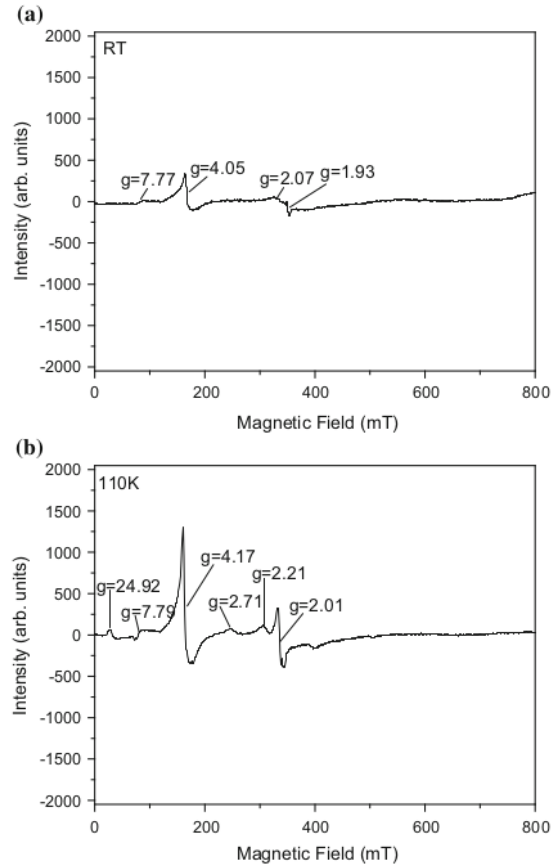


**Fig. 4** The EPR spectrum of $CeO_2$:$Fe^{3+}$ at **a** room temperature and **b** 110 K

$Fe^{3+}$ species in poly crystalline solids often deviate significantly from 2.0023. When $Fe^{3+}$ ions are placed in a ligand field environment, the $^6S_{5/2}$ ground state splits into three Kramers' doublets |±1/2>, |±3/2> and |±5/2>. The resonance signal at g = ~4.05, 4.17 arises from the middle Kramers' doublet |±3/2 > for $Fe^{3+}$ ions in almost completely rhombic environments with the ratio of the zero-field splitting parameters |E|/|D| ≈ 1/3 [40, 41]. The g values close to g ~ 2.0 is due to $Fe^{3+}$ ions in octahedral symmetry. The large number of g values obtained in the present case at RT and 110 K. It is most likely due to anisotropic nature of $Fe^{3+}$ ions in $CeO_2$ host. The g ~ 2.0 resonance signal may be attributed to either $Fe^{3+}$ ions interacting by dipole–dipole interaction in distorted octahedral field or to their super exchange interactions within the pairs of Fe ions [42, 43]. These large number of g values indicate that the iron ions are in trivalent state and the site symmetry is distorted octahedral. In the present case, EPR signal is not observed for $Fe^{2+}$ ions. It is known

that in the case of iron, both (2+ and 3+) redox states can potentially be EPR active, although the 2+ state normally is not. Sivaramaiah et al. [44] studied EPR studies of $Fe^{3+}$ ions in amethyst. They observed two broad signals at g = 10.8, 4.0 and one sharp signal at g = 2.002. The broad signals have been attributed to $Fe^{3+}$ clusters on surfaces. The sharp signal has been attributed to oxygen vacancy center $E_1'$. Sivaramaiah and Pan [45] studied thermodynamic and magnetic properties of surface $Fe^{3+}$ ions on quartz. They observed three resonance signals at g = 2.00, 4.28 and 15. The resonance signal at g = 4.28 is attributed to the substitutional $Fe^{3+}$ ions at the Si site. The signal at g = 2.00 has been attributed to oxygen vacancy center $E_1'$. The signal at g = 15 has been attributed to $Fe^{3+}$ clusters. The remarkable feature observed for this sample is that the optical spectrum observed due to $Fe^{3+}$ as well as $Fe^{2+}$ whereas EPR signal is due to $Fe^{3+}$ only.

### 3.4.1 Absolute number of spins

The absolute number of spins (N) participating in resonance can be calculated by comparing the area under the absorption curve with that of a standard of known concentration. Weil and Bolton [46] gave the following formula including the experimental parameters of both the sample and the standard

$$N = \frac{A_x(\mathrm{scan}_x)^2 G_{std}(B_m)_{std}(g_{std})^2[S\ (S+1)]_{std}(N_{std})}{A_{std}(\mathrm{scan}_{std})^2 G_x(B_m)_x(g_x)^2[S\ (S+1)]_x}, \quad (2)$$

where A is the area under the absorption curve, which is obtained from double integration of the first derivative spectrum, scan is the magnetic field corresponding to unit length of the spectrum, G is the gain, $B_m$ is the modulation amplitude, g is the g factor, S is the spin of the system in its ground state (S = 5/2 and 1/2 for $Fe^{3+}$ and $Cu^{2+}$, respectively). $N_{std}$ denotes the number of spins in 100 mg of $CuSO_4{\cdot}5H_2O$ standard. The absolute number of spins for the $Fe^{3+}$ signal at g = 4.05, 4.17 in $CeO_2$ was found to be order of $10^{19}$ spins/$m^3$ at RT and 110 K. This spin order is consistent with the spin order reported in the literature [36].

### 3.4.2 Gibbs free energy

The Gibbs free energy (ΔG) can be calculated using the following equation [44, 45]

$$\Delta G = 2.303\ RT\ \log_{10}(k_B T/\lambda h) \quad (3)$$

Here 'ΔG' is the Gibbs free energy, 'R' is the universal gas constant, '$k_B$' is the Boltzmann constant, 'T' is the absolute temperature, 'λ' is the rate constant, is equal to the absolute number of spins per $m^3$, and 'h' is Planck's constant. The Gibbs free energy of $CeO_2$:$Fe^{3+}$ is found to be −43.16 and −16.34 kJ/mol at RT and 110 K, respectively. Thus the stability of this sample is high at RT as Gibbs free energy is low at RT. Lower the Gibbs free energy value, higher the stability. The negative sign indicates that exothermic reaction takes place between the dopant and the host lattice and there is strong attraction between the dopant and the lattice.

### 3.4.3 Magnetic susceptibility

The magnetic susceptibility χ for the g = 4.05, 4.17 signals can be determined using the following expression [47, 48]

$$\chi = (Ng^2\beta^2 J(J+1))/3k_B T, \quad (4)$$

where N is the number of spins per $m^3$, g is the g factor and is equal to 4.05, 4.17, β is the Bohr magneton, S is the spin quantum number of unpaired electron = 5/2, $k_B$ is Boltzmann constant and T is absolute temperature. Using the above equation, the magnetic susceptibility of the sample at RT was found to be $20.46 \times 10^{-5}$ $m^3$/kg. Its value at 110 K was found to be $10.25 \times 10^{-4}$ $m^3$/kg. The calculated magnetic susceptibility values are consistent with the values reported in the literature [44, 45]. The advantage of this EPR method is that the diamagnetic contribution of magnetic susceptibility can be eliminated. For paramagnetic contribution of the sample, the magnetic susceptibility is calculated.

### 3.4.4 Curie constant

The empirical Curie constant can be found using the following expression [47, 48]

$$C = \frac{Ng^2\beta^2 J(J+1)}{3k_B}, \quad (5)$$

where N is number of spins/$m^3$, g = 4.05, 4.17, β is Bohr magneton, J is total angular momentum quantum number, $k_B$ is Boltzmann constant. The Curie constant was found to

**Table 1** The g values, number of spins (N), Gibbs free energy (ΔG), magnetic susceptibility (χ), Curie constant (C) and effective magnetic moment ($\mu_{eff}$) for $CeO_2$:$Fe^{3+}$ at RT and 110 K

| T (K) | g value | N (spins/$m^3$) | ΔG (kJ/mol) | χ ($m^3$/kg) | C (emu/mol) | $\mu_{eff}$ ($\mu_B$) |
|---|---|---|---|---|---|---|
| RT | 4.05 | $20.59 \times 10^{19}$ | −43.16 | $20.46 \times 10^{-5}$ | 0.061 | 11.9 |
| 110 | 4.17 | $97.29 \times 10^{19}$ | −16.34 | $10.25 \times 10^{-4}$ | 0.30 | 12.18 |

be 0.061 and 0.30 emu/mol at RT and 110 K, respectively. The Curie constant has increased with the decrease of temperature which demonstrates that the paramagnetic interactions increase with the decrease of temperature. The Curie constant indicates the nature of magnetic interactions and the low value of this constant is attributed to high antiferromagnetic interactions. It may also be attributed to the formation of $Fe^{3+}$–$Fe^{3+}$ ions pairs, if the exchange coupling between these ions is antiferromagnetic in nature, which is expected to result in a reduction of the Curie constant [49].

### 3.4.5 *Experimental effective magnetic moment*

The experimental effective magnetic moment can be determined using the following expression [50]

$$\mu\text{eff} = \frac{\sqrt{3k_B C}}{\sqrt{N}}, \tag{6}$$

where $k_B$ is Boltzmann constant, C is Curie constant, N is number of spins/$m^3$. The theoretical magnetic moment value for free $Fe^{3+}$ is 5.92 $\mu_B$. The experimental values were estimated to be 11.9 and 12.18 $\mu_B$ at RT and 110 K, respectively. The high value at both the temperatures indicates that ferromagnetic interactions are dominant in this sample. The high value also indicates that clusters of high spin $Fe^{3+}$ are found in this sample. Table 1 shows the g values, number of spins (N), Gibbs free energy ($\Delta G$), magnetic susceptibility ($\chi$), Curie constant (C) and effective magnetic moment ($\mu_{eff}$) for $CeO_2$:$Fe^{3+}$ powder at RT and 110 K.

## 4 Conclusions

Fe doped $CeO_2$ was successfully prepared by the combustion synthesis method. The XRD revealed the presence of single phase of $CeO_2$. Scanning electron microscope images of prepared powders showed an agglomeration. Absorption spectrum studies on the Fe doped $CeO_2$ sample show two main broad absorption bands observed at around 535 nm and 906 nm which is the characteristic of $Fe^{3+}$ and $Fe^{2+}$ ions in octahedral and tetrahedral symmetries, respectively. The weak band centered at around 671 nm is due to $Fe^{3+}$ ions in octahedral symmetry. EPR spectrum of Fe doped $CeO_2$ sample showed multiple resonance signals having at least 6 'g' values. These resonance signals can be attributed to $Fe^{3+}$ ions. The number of g values is attributed to anisotropic nature of this sample.

**Acknowledgments** This paper was supported by the KU Research Professor Program of Konkuk University.

## References


1. S. De, S. Mohanty, S.K. Nayak, Bioprocess. Biosyst. Eng. **38**, 1671–1683 (2015)
2. M.M. Khan, S.A. Ansari, D. Pradhan, D.H. Han, J. Lee, M.H. Cho, Ind. Eng. Chem. Res. **53**, 9754–9763 (2014)
3. P. Knauth, J. Engel, S.R. Bishop, H.L. Tuller, J. Electroceram. **34**, 82–90 (2015)
4. C. Slostowski, S. Marre, O. Babot, T. Toupance, C. Aymonier, Langmuir **30**, 5965–5972 (2014)
5. [illegible] Zheng, L. Liu, X. Zhou, Colloid J. **76**, 558–563 (2014)
6. M. Mogensen, N.M. Sammes, G.A. Tompsett, Solid State Ionics **129**, 63–94 (2000)
7. H.L. Tuller, A.S. Nowick, J. Phys. Chem. Solids **38**, 859–867 (1977)
8. H. Inaba, H. Tagawa, Solid State Ionics **83**, 1–16 (1996)
9. T. Mori, T. Kobayashi, Y. Wang, J. Drennan, T. Nishimura, J.G. Li, H. Kobayashi, J. Am. Ceram. Soc. **88**, 1981–1984 (2005)
10. Y. Cao, H. Li, X. Li, L. Wang, G. Zhu, Q. Tang, Chin. J. Chem. Eng. **23**, 446–450 (2015)
11. S.B. Khan, M. Faisal, M.M. Rahman, A. Jamal, Sci. Total Environ. **409**, 2987–2992 (2011)
12. W. Deng, D. Chen, L. Chen, Ceram. Int. **41**, 11570–11575 (2015)
13. T. Feng, X. Wang, G. Feng, Mater. Lett. **100**, 36–39 (2013)
14. H.S. Potdar, S.B. Deshpande, Y.B. Khollam, A.S. Deshpande, [illegible] Date, Mater. Lett. **57**, 1066–1071 (2003)
15. H.S. Potdar, S.B. Deshpande, A.S. Deshpande, S.P. Gokhale, S.K. Date, Y.B. Khollam, A.J. Patil, Mater. Chem. Phys. **74**, 306–312 (2002)
16. X. Liu, J. Ding, X. Lin, R. Gao, Z. Li, W.-L. Dai, Appl. Catal. A **503**, 117–123 (2015)
17. J.-H. Lee, S.M. Yoon, B.-K. Kim, H.-W. Lee, H.S. Song, J. Mater. Sci. **37**, 1165–1171 (2002)
18. T. Wang, O. Sel, I. Djerdj, B. Smarsly, Colloid Polym. Sci. **285**, 1–9 (2006)
19. I. Luisetto, S. Tuti, C. Battocchio, S.L. Mastro, A. Sodo, Appl. Catal. A **500**, 12–22 (2015)
20. A. Beltram, M. Melchionna, T. Montini, L. Nasi, R.J. Gorte, M. Prato, P. Fornasiero, Catal. Today **253**, 142–148 (2015)
21. P. Djinović, J. Batista, J. Levec, A. Pintar, Appl. Catal. A **364**, 156–165 (2009)
22. M. Boaro, A. Pappacena, C. Abate, M. Ferluga, J. Llorca, A. Trovarelli, J. Power Sources **270**, 79–91 (2014)
23. X. Yang, L. Yang, S. Lin, R. Zhou, J. Hazard. Mater. **285**, [illegible]2–189 (2015)
24. [illegible] Yue, X.-M. Zhang, J. Alloys Compd. **475**, 702–705 (2009)
25. L. Truffault, Q.W. Yao, D. Wexler, I.P. Nevirkovets, K. Konstantinov, T. Devers, J. Nanosci. Nanotechnol. **11**, 4019–4028 (2011)
26. W. Tiebao, C. Chunxiang, W. Xiaodong, L. Guobin, J. Nanomater. (2010), Article ID 768251, 5 p
27. M. Radović, Z. Dohčević-Mitrović, A. Golubović, V. Fruth, S. Preda, M. Šćepanović, Z.V. Popović, Ceram. Int. **39**, 4929–4936 [illegible]013)
28. Y. Wang, F. Wang, Y. Chen, D. Zhang, B. Li, S. Kang, X. Li, L. Cui, Appl. Catal. B Environ. **147**, 602–609 (2014)
29. R.S. Muralidhara, C.R. Kesavulu, J.L. Rao, R.V. Anavekar, R.P.S. Chakradhar, J. Phys. Chem. Solids **71**, 1651–1655 (2010)
30. R.P. Sreekanth Chakradhar, G. Sivaramaiah, J. Lakshmana Rao, N.O. Gopal, Spectrochim. Acta A Mol. Biomol. Spectrosc. **62**, [illegible]57 (2005)
31. I. Ardelean, M. Peteanu, S. Flip, V. Simon, G.D. Gyorffy, Solid State Commun. **102**, 341–346 (1997)
32. L.B. Glebov, E.N. Boulos, J. Non-Cryst. Solids **242**, 49–62 (1998)

33. P.A. Bingham, J.M. Parker, T.M. Searle, I. Smith, J. Non-Cryst. Solids **353**, 2479–2494 (2007)
34. B. Mehdikhani, G.H. Borhani, Process. Appl. Ceram. **7**, 117–121 (2013)
35. R. Klement, J. Kraxner, M. Liska, Ceram. Silik. **53**, 180–183 (2009)
36. S.P. Singh, R.P.S. Chakradhar, J.L. Rao, B. Karmakar, J. Alloys Compd. **493**, 256–262 (2010)
37. F. Marabelli, P. Wachter, Phys. Rev. B **36**, 1238–1243 (1987)
38. E. Wuilloud, B. Delley, W.D. Schneider, Y. Baer, Phys. Rev. Lett. **53**, 202–205 (1984)
39. B. Bleany, K.W.H. Stevens, Rep. Prog. Phys. **16**, 108–159 (1953)
40. R.M. Golding, T. Singhasuwich, W.C. Tennant, Mol. Phys. **34**, 1343–1350 (1978)
41. Y. Pan, M. Mao, J. Lin, Can. Mineral. **47**, 933–945 (2009)
42. I. Ardelean, P. Pascuta, L.V. Giurgiu, Int. J. Mod. Phys. B **17**, 3049–3056 (2003)
43. E. Burzo, I. Ardelean, I. Ursu, J. Mater. Sci. **15**, 581–593 (1980)
44. G. Sivaramaiah, J. Lin, Y. Pan, Phys. Chem. Miner. **38**, 159–167 (2011)
45. G. Sivaramaiah, Y. Pan, Phys. Chem. Miner. **39**, 515–523 (2012)
46. J.A. Weil, J.R. Bolton, *Electron Paramagnetic Resonance: Elementary Theory and Practical Applications* (Wiley, New York, 2007)
47. A.J. Dekker, *Solid State Physics*. Department of Electrical Engineering, University of Groningen, Netherlands (2006)
48. C. Kittel, *Introduction to Solid State Physics*, 7th edn. (Wiley, New York, 1996)
49. M. Borgheresi, F. Di Benedetto, A. Caneschi, G. Pratesi, M. Romanelli, L. Sorace, Phys. Chem. Miner. **34**, 609–619 (2007)
50. A.M. Hashem, H.M. Abuzeid, D. Mikhailova, H. Ehrenberg, A. Mauger, C.M. Julien, J. Mater. Sci. **47**, 2479–2485 (2012)

# Combustion synthesized Fe doped CeO2 powder-characterization, optical absorption and EPR spectroscopy

ORIGINALITY REPORT

| 16% | 12% | 16% | 5% |
|---|---|---|---|
| SIMILARITY INDEX | INTERNET SOURCES | PUBLICATIONS | STUDENT PAPERS |

PRIMARY SOURCES

| | | |
|---|---|---|
| 1 | connection.ebscohost.com<br>Internet Source | 1% |
| 2 | Raunak Kumar Tamrakar, D. P. Bisen, Kanchan Upadhyay, Ishwar Prasad Sahu, Nameeta Brahme. "Effect of synthesis annealing temperature & Yb3+ concentration on photoluminescence properties of monoclinic Gd2O3 phosphor", Journal of Optics, 2015<br>Publication | 1% |
| 3 | R.V.S.S.N. Ravikumar, Ryuichi Komatsu, Ko. Ikeda, A.V. Chandrasekhar, B.J. Reddy, Y.P. Reddy, P.S. Rao. "Electron paramagnetic resonance and optical absorption spectra of Cr3+ ions in cadmium phosphate glass", Solid State Communications, 2003<br>Publication | 1% |
| 4 | Submitted to TechKnowledge<br>Student Paper | 1% |

repositorium.sdum.uminho.pt

| | | |
|---|---|---|
| 5 | Internet Source | 1 % |
| 6 | www.ijera.com<br>Internet Source | 1 % |
| 7 | Reham M. M. Morsi, Safeya Ibrahim, Morsi M. Morsi. "Characterization of sodium lead silicate glasses containing low and high levels of Fe2O3 and effect of its replacement for Na2O", Journal of Materials Science: Materials in Electronics, 2017<br>Publication | 1 % |
| 8 | Ke Yang, Dong-Feng Li, Wei-Qing Huang, Liang Xu, Gui-Fang Huang, Shuangchun Wen. "Origin of enhanced visible-light photocatalytic activity of transition-metal (Fe, Cr and Co)-doped CeO2: effect of 3d orbital splitting", Applied Physics A, 2016<br>Publication | 1 % |
| 9 | Submitted to University of KwaZulu-Natal<br>Student Paper | 1 % |
| 10 | Singh, Vijay, Vineet Kumar Rai, V. Venkatramu, R.P.S. Chakradhar, and Sang Hwan Kim. "Infrared emissions in MgSrAl10O17:Er3+ phosphor co-doped with Yb3+/Ba2+/Ca2+ obtained by solution combustion route", Journal of Luminescence, 2013.<br>Publication | 1 % |

| | | |
|---|---|---|
| 11 | Submitted to King Saud University<br>Student Paper | 1 % |
| 12 | M.S. Bhagat, K.N. Shinde, N. Singh, M.S. Pathak, Pramod K. Singh, S.U. Pawar, Vijay Singh. "Photoluminescence properties of green emitting CaY 2 Al 4 SiO 12 :Tb 3+ garnet phosphor", Optik, 2018<br>Publication | 1 % |
| 13 | www.mysciencework.com<br>Internet Source | 1 % |
| 14 | HARA, Akihiro, Yoshihiro HIRATA, Soichiro SAMESHIMA, Naoki MATSUNAGA, and Teruhisa HORITA. "Grain size dependence of electrical properties of Gd-doped ceria", Journal of the Ceramic Society of Japan, 2008.<br>Publication | 1 % |
| 15 | naac.msubaroda.ac.in<br>Internet Source | 1 % |
| 16 | research-repository.st-andrews.ac.uk<br>Internet Source | 1 % |
| 17 | www.irjet.net<br>Internet Source | 1 % |
| 18 | Bernardi, M. I. B., A. Mesquita, F. Béron, K. R. Pirota, A. O. de Zevallos, A. C. Doriguetto, and H. B. de Carvalho. "The role of oxygen vacancies and their location in the magnetic | 1 % |

properties of Ce1−xCuxO2−δ nanorods", Physical Chemistry Chemical Physics, 2014.
Publication

| | | |
|---|---|---|
| 19 | I. Ardelean, P. Păşcuţă, L. V. Giurgiu. " EPR and Magnetic Susceptibility Investigations of - - Glasses ", International Journal of Modern Physics B, 2012<br>Publication | 1 % |
| 20 | slideheaven.com<br>Internet Source | 1 % |
| 21 | ebin.pub<br>Internet Source | 1 % |
| 22 | "Spectroscopic Methods in Mineralogy and Material Sciences", Walter de Gruyter GmbH, 2014<br>Publication | 1 % |
| 23 | T. Caillot, Z. Salama, N. Chanut, F.J. Cadete Santos Aires, S. Bennici, A. Auroux. "Hydrothermal synthesis and characterization of zirconia based catalysts", Journal of Solid State Chemistry, 2013<br>Publication | 1 % |
| 24 | www.iosrjen.org<br>Internet Source | 1 % |

| | | | |
|---|---|---|---|
| Exclude quotes | Off | Exclude matches | < 1% |
| Exclude bibliography | Off | | |